

Improved Droop Control Strategy for Grid-Connected Inverters

Abusara, Mohammad; Sharkh, Suleiman; Guerrero, Josep M.

Published in:
Sustainable Energy, Grids and Networks

DOI (link to publication from Publisher):
[10.1016/j.segan.2014.10.002](https://doi.org/10.1016/j.segan.2014.10.002)

Publication date:
2015

Document Version
Early version, also known as pre-print

[Link to publication from Aalborg University](#)

Citation for published version (APA):
Abusara, M., Sharkh, S., & Guerrero, J. M. (2015). Improved Droop Control Strategy for Grid-Connected Inverters. *Sustainable Energy, Grids and Networks*, 1, 10-19. <https://doi.org/10.1016/j.segan.2014.10.002>

General rights

Copyright and moral rights for the publications made accessible in the public portal are retained by the authors and/or other copyright owners and it is a condition of accessing publications that users recognise and abide by the legal requirements associated with these rights.

- Users may download and print one copy of any publication from the public portal for the purpose of private study or research.
- You may not further distribute the material or use it for any profit-making activity or commercial gain
- You may freely distribute the URL identifying the publication in the public portal -

Take down policy

If you believe that this document breaches copyright please contact us at vbn@aub.aau.dk providing details, and we will remove access to the work immediately and investigate your claim.

Improved Droop Control Strategy for Grid-Connected Inverters

Mohammad A. Abusara, Suleiman M. Sharkh, and Josep M. Guerrero

Abstract – An improved control strategy for grid-connected inverters within microgrids is presented in this paper. The strategy is based on the classical $P-\omega$ and $Q-V$ droop method. The improvement in the proposed control strategy is twofold: Firstly, the transient response of the droop controller is improved by replacing the traditional method of measuring average power, which is based on using a first order low pass filter, by a real time integration filter. This is shown to reduce the imported transient energy when connecting to the grid. Secondly, the steady state output current quality is improved by utilising a virtual inductance, which is shown to reject grid voltage harmonics disturbance and thus improve the output current THD. A small signal model of the inverter based on the transfer function approach is developed to analyse its stability and determine droop gains. Simulation and experimental results are presented to validate the model and demonstrate the controller capabilities.

Index Terms – Droop control, microgrid, grid-connected inverters.

I. INTRODUCTION

The use of frequency and voltage droop method to control power sharing of parallel and grid-connected PWM inverters is well established in the literature [1]-[16]. This method requires active and reactive power to be measured in order to droop the frequency and voltage accordingly such that the inverter mimics the behaviour of a synchronous generator. In reported systems [2]-[12], a low pass first order filter is used to obtain the average power from single phase instantaneous power measurement. In a balanced three phase system, the instantaneous power equals the average power and such a filter might not be necessary. However, in an unbalanced three-phase system, the instantaneous power has a ripple component and a filter becomes essential to prevent the ripple component from propagating to the frequency and amplitude through the droop control feedback. However, this filter has a significant effect on the dynamics of the droop controller due to associated phase lag [12]. In [13], [25] and [26] the average power was measured by integrating the instantaneous power. However, no discussion regarding the advantage of this method over the low pass filter was provided. In this paper it is shown that the real time integration method for calculating average power gives superior controller dynamic performance compared to the low pass filter method.

When droop control is used for grid-connected inverters, the current injected into the grid is basically controlled by adjusting the power angle, and hence, there is no direct control over the quality of the output current in contrast to traditional current mode grid-connected inverters [17]-[19] where the control is performed using a feedback signal of the output current. In the presence of grid voltage harmonics, harmonic currents will flow from/to the inverter due to its low output impedance of the inverter and its output filter. In grid-connected inverters, an *LCL* filter is normally used (rather than *LC*) as shown in Fig. 1. The grid side inductor L_2 is used to block the high switching frequency component of the output current from being injected into the grid. The presence of L_2 increases the output impedance of the inverter and to a certain extent it improves the output current Total Harmonic Distortion (THD). However, the design criterion for choosing the inductance of L_2 is to block the high switching frequency current [18],[19] and hence L_2 is normally chosen to be relatively small (increasing L_2 will increase size and cost). The other disadvantage of increasing L_2 is that it worsens the voltage THD when the inverter operates in island mode and supplies a non-linear load. In this paper, a virtual inductance is proposed to further increase the output impedance of the inverter but without compromising size and cost. This virtual inductance can be deactivated or reduced in standalone island mode so it does not affect the voltage THD when supplying a non-linear load. The use of virtual impedance has in fact been proposed in the literature [2],[3], [5]-[7] but it has been proposed for inverters operating in standalone parallel mode to guarantee a predominant inductive output impedance of paralleled inverter so that the active power is predominantly determined by the power angle and the reactive power is predominantly determined by the voltage amplitude. The main motivation, however, for using the virtual inductance in this paper is to improve the quality of the output current in grid-connected mode. Although some previous publications discussed the effect of grid side inductance on the controller stability of grid-connected inverters [19]-[21], they only considered the effect of physical inductance. Also, in such grid-connected systems, the inverter is typically controlled as a current source injecting certain amount of current into the grid. In this paper, however, the effect of a virtual inductance on the stability of grid connected inverters, based on droop-control, is discussed taking into account the effect of the low pass filter required for practical implementation. The model (current-voltage transfer function) of a virtual inductor is different from a physical inductor.

Several publications have proposed small signal models for droop controlled inverters operating in grid-connected mode [22]-[24]. These models used state-space equations to describe the inverter dynamics. In this paper, an intuitive model based on the transfer function approach is presented. The model is used to analyse stability and choose the droop coefficients.

Applications such as photovoltaic single-phase micro-inverters have used droop control in order to achieve a flexible operation of both grid-connected and island modes [13], [27]-[29]. Although small-signal analysis have been done for droop-

controlled grid-connected inverters powered by ideal DC sources, to the best knowledge of the authors, still there are no studies on how the droop controller affects the DC-link voltage especially when the inverter first connects to the grid.

The main novel contributions of the paper are: 1) A detailed investigation, not reported before in the literature, of the effect of average power measurement techniques (low pass filtering and integration of instantaneous power methods) on the performance of the power flow controller; the integration method is shown to be superior, 2) Using virtual inductance as an effective method to reduce current THD and investigate its practical realisation using a high-pass filter and its effect on stability and current THD; previous work in the literature, including our own, only considered the effect of physical inductance on stability and THD 3) A new intuitive small signal model of a droop controlled grid connected inverter based on transfer function approach, 4) a study of the impact of the droop controller on DC-link voltage, which has not been considered before in the literature.

The paper is organized as follow. Section II gives an overview of the system. Section III discusses the inner loop controller of the inverter. In section IV, the development of a small signal model of the inverter and the design of the droop control are presented. Simulation and experimental results are presented in sections V and VI, respectively.

II. SYSTEM OVERVIEW

The grid-connected inverter considered in this paper is shown in Fig. 1. It consists of a three-phase half bridge inverter with *LCL* filter. The inverter parameters are given in Table I. The inverter controller is illustrated in Fig. 2. It consists of an outer power flow controller that sets the voltage amplitude and frequency demand for an inner voltage inner loop controller. The power flow controller regulates the amount of active and reactive power injected into the grid. The voltage inner loop controller regulates the capacitor voltage V_c by utilising two feedback loops of the capacitor voltage and current. The detailed design of the inner loop controller is discussed in section III and the design of the power flow controller is discussed in section IV.

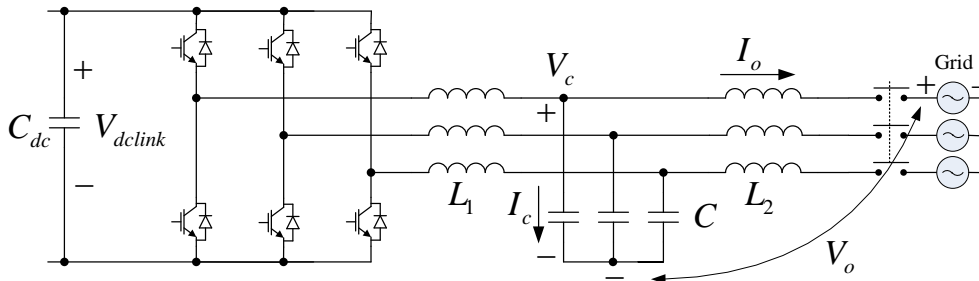


Fig. 1. Circuit diagram of the grid-connected inverter

TABLE I
INVERTER PARAMETER VALUES

Symbol	Value	Description
L_1	350 μ H	Inverter-side filter inductor
C	160 μ F	Filter capacitor
L_2	250 μ H	Grid-side filter inductor
C_{dc}	2mF	DC-link capacitor
P_{max}	60kW	Maximum active power rating
Q_{max}	45kVAR	Maximum reactive power rating

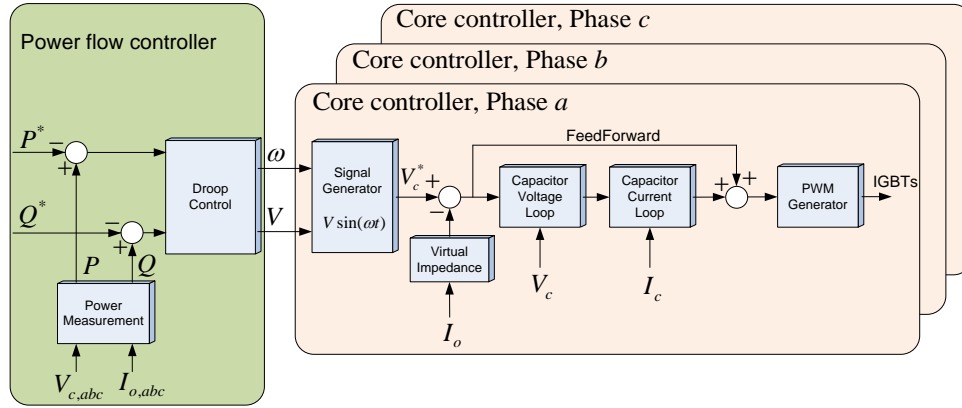


Fig. 2. Inverter controller

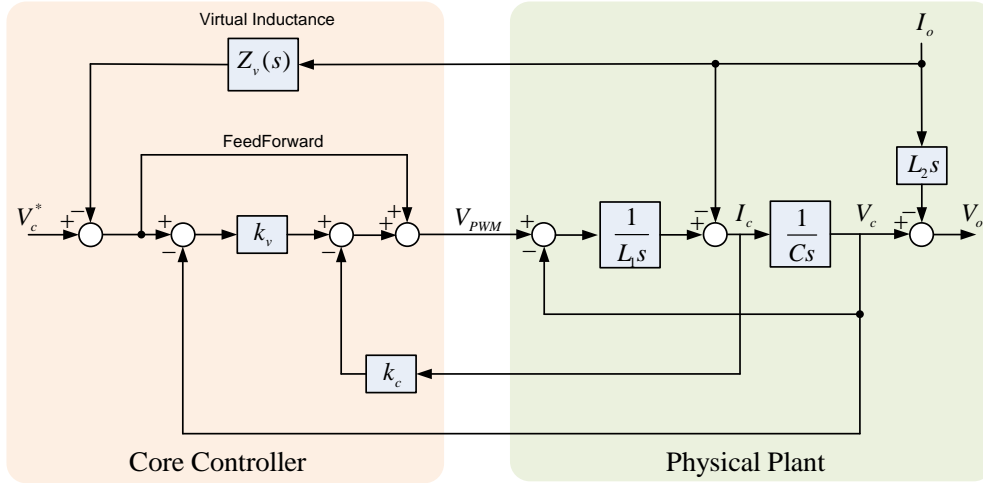


Fig. 3. Transfer function block diagram of one phase and its inner loop controller

III. INNER LOOP CONTROLLER

Fig. 3 shows the block diagram of one inverter phase and its inner loop controller. The controller is implemented in the abc frame. The controller could also be implemented in the dq rotating frame where a Proportional-Integral (PI) controller is equivalent to a Proportional Resonant (PR) controller in the stationary frame. It has been reported that implementing a PI controller in the dq frame is better than a PR controller in the stationary frame as the latter can lead to analytical errors especially at the low frequencies [31]. In this design, only proportional term will be used in the inner voltage controller. Therefore, the abc stationary frame is used for its simplicity. The inner loop voltage controller consists of an outer feedback loop of the capacitor voltage and an inner feedback loop of the capacitor current; the latter provides damping of filter resonance. A feedforward loop of the reference voltage is also implemented to improve the speed of response and minimise the steady state error.

Without the virtual inductance loop, the output voltage can be shown to be given by

$$V_o = G(s)V_c^* - Z(s)I_o \quad (1)$$

where $G(s)$ is the closed loop transfer function and $Z(s)$ is the system output impedance,

$$G(s) = \frac{k_v + 1}{L_1 C s^2 + k_c C s + k_v + 1} \quad (2)$$

$$Z(s) = \frac{L_1 s}{L_1 C s^2 + k_c C s + k_v + 1} + L_2 s \quad (3)$$

The voltage and current proportional gains k_v and k_c were chosen to be 2.0 and 2.2, respectively to provide good transient and steady state response. In terms of transient response, the aforementioned gains give a damping ratio $\zeta = k_c \sqrt{L_1 C / (k_v + 1)} / 2L_1 = 0.43$ and a step response settling time of about 1 m sec. The steady state response can be analysed using the bode diagram of $G(s)$ which is shown in Fig. 4. At the fundamental frequency $f = 50\text{Hz}$, the gain is 0.01dB and the phase lag is 2.12deg. This is a characteristic of the closed loop system, which also depends on system parameters uncertainty. The phase lag will cause the inverter to import some transient power when connecting to the grid as will be shown later.

Virtual Inductance and Grid harmonics Rejection

The ideal transfer function of a virtual inductance L_v is given by

$$Z_{vi}(s) = sL_v \quad (4)$$

However, implementing the derivative as in (4) experimentally introduces the well-known problem of noise amplification. Therefore, the pure derivative is replaced by a high-pass filter which is, in fact, a pure derivative preceded by a low pass filter. The transfer function of the virtual inductance is therefore given by

$$Z_v(s) = \frac{\omega_c s}{s + \omega_c} L_v \quad (5)$$

where ω_c is the cut-off frequency of the high pass filter. When the virtual inductance is implemented, the output voltage can be shown to be given by

$$V_o = G(s)V_c^* - Z_o(s)I_o \quad (6)$$

where $Z_o(s)$ is the inverter's modified output impedance and is given by

$$Z_o(s) = Z(s) + G(s)Z_v(s) \quad (7)$$

Equation (6) can be represented by the block diagram shown in Fig. 5. When the system is connected to the grid, the output voltage V_o is actually the grid voltage. To increase the system ability to reject grid voltage harmonics, it is desirable to maximise $Z_o(s)$ at these harmonics. The Bode diagrams of both $Z(s)$ and $Z_o(s)$ for $L_v = 650\mu\text{H}$ and 3 different values of ω_c are shown in Fig. 6. It can be noticed that $Z_o(s)$ provides higher output impedance and hence better grid harmonics rejection for frequencies up to 900Hz (the 18th harmonic). It can also be noticed that reducing ω_c will reduce impedance and hence provide lower grid harmonics rejection. For the frequency range from 1kHz to 3kHz, $Z_o(s)$ provides lower impedance than $Z(s)$. However, most of the dominant grid harmonics are in fact the lower ones (lower than 1kHz) where $Z_o(s)$ provides higher impedance than $Z(s)$.

From Fig. 5, the stability of the inner loop controller is guaranteed if both closed loop transfer functions $G(s)$ and $1/Z_o(s)$ are stable. The stability of $G(s)$ has been guaranteed by proper selection of the proportional gains k_v and k_c as discussed above. The stability of $1/Z_o(s)$ can be determined by examining the roots of the characteristic equation of $1/Z_o(s)$ which is given by

$$Z_o(s) = 0 \quad (8)$$

To analyse the effect of the virtual inductance on the stability of $1/Z_o(s)$, the root locus of (8) is plotted as shown in Fig. 7 with L_v varying from 0 to 2.5mH for 3 different cases of the cut-off frequency ($\omega_c = 1000, 1500$, and 2000 rad/s). As L_v increases, the dominant roots are pushed to the right and hence stability is reduced. In the magnified portion of the root locus diagram, it can be seen that increasing ω_c also decreases stability as the system becomes unstable for a smaller value of L_v . Therefore, increasing L_v and ω_c reduces stability but at the same time increases harmonics rejection by increasing the impedance gain over a higher frequency range as was shown from the bode diagram of Fig. 6. Therefore, the determination of L_v and ω_c is a compromise between stability and harmonics rejection. By choosing $L_v = 650\mu\text{H}$ and $\omega_c = 1500$ rad/sec, the dominant close loop poles give an acceptable damping ratio of 0.2 and settling time of 1.8ms. This design provides high impedance at most significant grid harmonics (up to the 18th harmonic). As a result the system's ability to reject grid voltage harmonics increases. The system's ability to reject grid voltage disturbance can be simply evaluated from (6) by calculating the transfer function I_o/V_o when V_c^* is set to zero. In this case, $I_o/V_o = -1/Z_o(s)$. At different grid harmonics h , the disturbance rejection is calculated as $1/|Z_o(j2\pi h)|$. Table II shows the disturbance rejection at the odd grid harmonics up to the 17th harmonic without virtual inductance ($L_v = 0$) and with virtual inductance ($L_v = 650\mu\text{H}$). It is quite clear that the virtual inductance greatly improves disturbance rejection.

The Bode diagram in Fig. 6 shows predominant inductive impedance in the vicinity of the fundamental frequency. Thus, the output impedance (around the fundamental frequency) can be approximated as

$$Z_o(s) \approx L_o s \quad (9)$$

where L_o is the effective output inductance of the system that will be used in the following section. Its value from the Bode diagram of $Z_o(s)$ is $L_o = 996\mu\text{H}$.

Equation (6) can be represented by the Thévenin's equivalent circuit shown in Fig. 8(a). Because $G(s)$ has a relatively fast response settling time ($\sim 1\text{ms}$) with respect to that of the outer droop controller, it can be assumed to be an ideal voltage source with settable magnitude and frequency. Therefore, the grid-connected inverter can now be represented by an ideal voltage source in series with an inductor L_o as shown in Fig. 8(b).

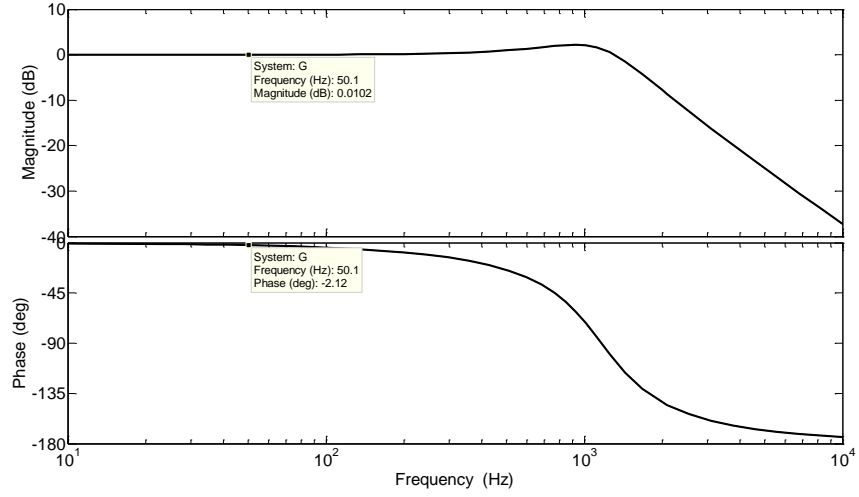


Fig. 4. Bode diagram of $G(s)$.

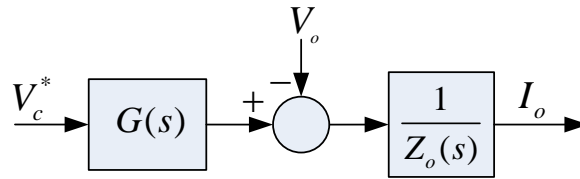


Fig. 5. Closed loop transfer functions relating I_o to V_c^* and V_o .

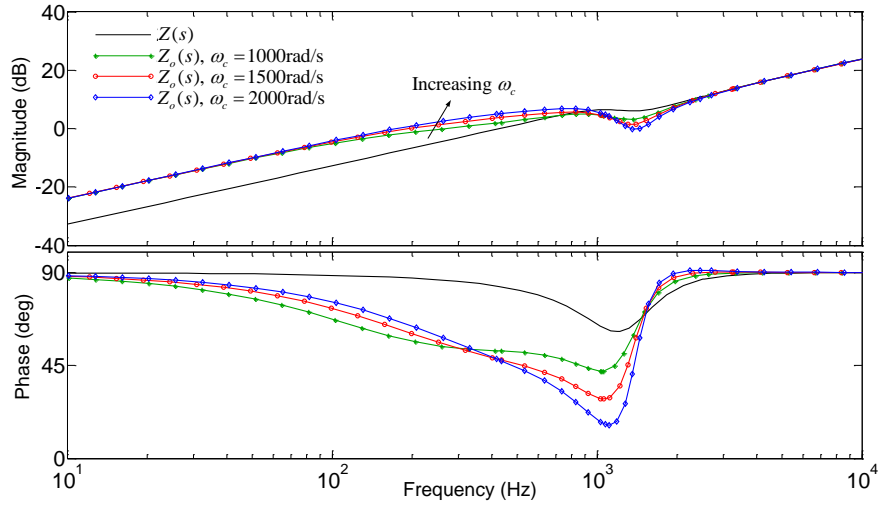


Fig. 6. Bode diagram of output impedance.

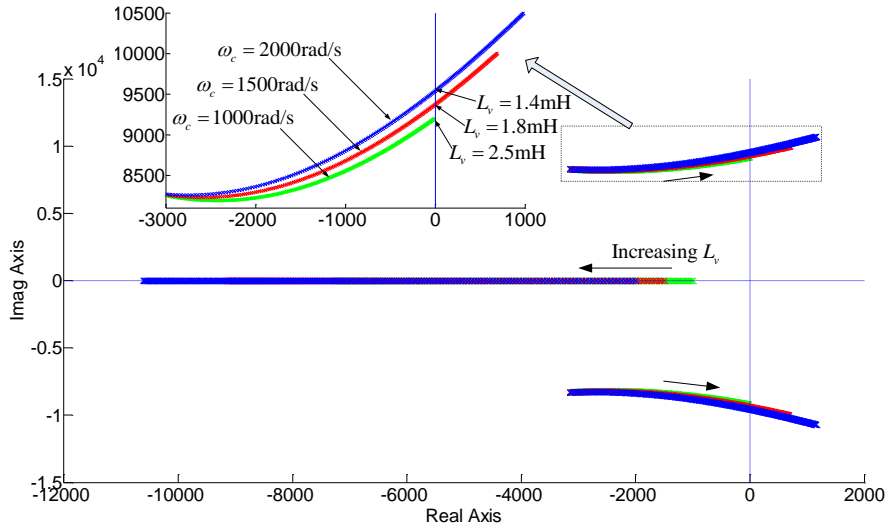


Fig. 7. Root locus of the characteristic equation $Z_o(s) = 0$ with L_v varying from 0 to 2.5mH for three different values of ω_c : 1000, 1500, 2000 rad/s.

TABLE II
GRID DISTURBANCE REJECTION

Harmonic (h)	$1/ Z_o(j2\pi h) $ (dB) $L_v = 0\mu H$	$1/ Z_o(j2\pi h) $ (dB) $L_v = 650\mu H$
3	9.22	1.63
5	4.76	-1.33
7	1.78	-2.88
9	-0.43	-3.92
11	-2.21	-4.69
13	-3.64	-5.27
15	-4.80	-5.61
17	-5.64	-5.65

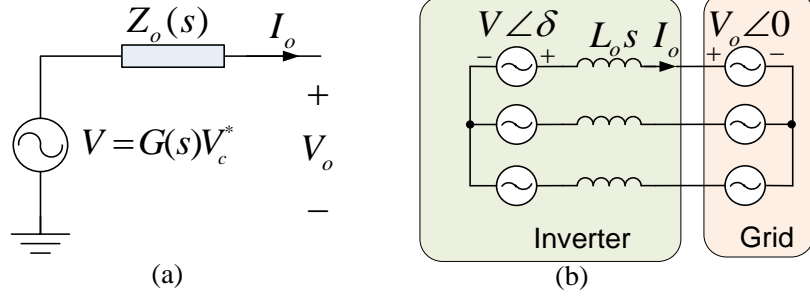


Fig. 8. Thévenin's equivalent circuit diagram of grid-connected inverter (a) single phase, (b) three-phase.

IV. DESIGN OF POWER FLOW CONTROLLER

A. Droop Control Equations

The proposed droop control is given by

$$\omega = \omega_o^* - (k_\omega + k_{\omega_I}/s)(P - P^*) \quad (10)$$

$$V = V_o^* - (k_a + k_{a_I}/s)(Q - Q^*) \quad (11)$$

where ω_o^* , V_o^* are the nominal frequency and voltage references, respectively. k_ω , and k_a are the proportional frequency and voltage droop coefficients, respectively. k_{ω_I} , and k_{a_I} are the integral frequency and voltage droop coefficients, respectively. During steady state, the inverter runs at the same frequency as that of the grid, $\omega = \omega_o$ (transient frequencies might be different). Similarly, the inverter voltage will nearly equal the grid voltage plus the small voltage drop across the inverter output impedance, i.e., $V \approx V_o$. Assuming that the grid frequency and voltage equal their nominal values used by the controller such that $\omega_o = \omega_o^*$ and $V_o = V_o^*$, then according to (10) and (11), $P = P^*$ and $Q = Q^*$ even if the integral droop coefficients k_{ω_I} , k_{a_I} are set to zero. However, the grid frequency and voltage can vary with time due to variation of active and reactive loads, or the connection or disconnection of big generators. If the grid frequency and voltage do not equal their nominal reference values used by the inverter controller such that $\omega_o \neq \omega_o^*$ and $V_o \neq V_o^*$ then the inverter will produce active and reactive power that are different from those of the set points. Typically, the grid frequency can change by 2% and the grid voltage can change by 10%, which can result in significant deviations of the inverter's output active and reactive power from the set points. To overcome this problem, the basic conventional proportional droop controller is modified to a PI controller to

eliminate these power steady state errors as was shown in (10) and (11). As this inverter will operate in grid-connected mode, there is no concern of frequency and voltage drifting as a result of using the integral term in the droop controller because the output frequency and voltage of the inverter will be fixed by the stiff grid. Usually the grid voltage and frequency do not vary very quickly and hence the response time of the integral parts of the PI controllers can be relatively slow, but it needs to be fast enough to track changes in grid frequency and voltage [26].

B. Small Signal Model

An equivalent circuit diagram of the grid-connected inverter was shown in Fig. 8(b). The grid impedance was neglected as the inverter output impedance is usually much higher than the grid impedance. The active and reactive power flow between the inverter and the grid can be shown to be given by

$$P = \frac{3V_o \sin \delta}{\omega_o L_o} \quad (12)$$

$$Q = \frac{3(V_o \cos \delta - V_o^2)}{\omega_o L_o} \quad (13)$$

A small change \tilde{P} and \tilde{Q} in active and reactive power, respectively, are given by

$$\tilde{P} = 3 \frac{V_o}{\omega_o L_o} (\sin \delta_{eq} \tilde{V} + V_{eq} \cos \delta_{eq} \tilde{\delta}) \quad (14)$$

$$\tilde{Q} = 3 \frac{V_o}{\omega_o L_o} (\cos \delta_{eq} \tilde{V} - V_{eq} \sin \delta_{eq} \tilde{\delta}) \quad (15)$$

where δ_{eq} and V_{eq} are the equilibrium points around which the small signal analysis is performed. By perturbing (10) and (11) we get

$$\tilde{\omega} = \tilde{\omega}_o + (k_\omega + k_{\omega_I}/s)(\tilde{P}^* - \tilde{P}_{avg}) \quad (16)$$

$$\tilde{V} = \tilde{V}_o + (k_a + k_{a_I}/s)(\tilde{Q}^* - \tilde{Q}_{avg}) \quad (17)$$

where \tilde{P}_{avg} and \tilde{Q}_{avg} are small changes in the measured average active and reactive power, respectively. The grid frequency and voltage reference points ω_o^* and V_o^* are fixed by the controller. However, the grid frequency ω_o and voltage V_o may change slightly and hence the notations $\tilde{\omega}_o$ and \tilde{V}_o in (16) and (17) represent the small deviations in the grid frequency and voltage from their nominal values, respectively. The small signal model described by (14)-(17) can be represented by a block diagram as shown in Fig. 9 where the angle δ_o , represented as a disturbance, is the initial angle between the inverter voltage and the grid voltage before connection. It is mainly caused by the phase lag of the closed loop system as was shown in Fig. 4. The transfer function $F(s)$ is the power measurement transfer function that relates the average power to the instantaneous power. In a balanced three-phase system, the instantaneous total power is free from ripple. However, if the system is unbalanced, undesired ripple will appear in the instantaneous total power signal and a filter $F(s)$ has to be used. $F(s)$ can be a simple low pass filter, that is,

$$F(s) = \frac{\omega_f}{s + \omega_f} \quad (18)$$

The cutoff frequency of the low pass filter ω_f needs to be low enough to filter out the undesired terms but it needs to be high enough to give an adequately fast power measurement response time. It is common practice to select the cutoff frequency to be one decade below the fundamental frequency [3]. Alternatively, the average of the power can be calculated by integrating the instantaneous power over one fundamental cycle T using the following equations,

$$P_{avg} = \frac{1}{T} \int_{t-T}^t p(t) dt \quad (19)$$

$$Q_{avg} = \frac{1}{T} \int_{t-T}^t q(t) dt \quad (20)$$

where $p(t)$ and $q(t)$ are the instantaneous active and reactive power, respectively. The integration is rolled over the last fundamental cycle and is updated every time new voltage and current samples are available. In this case, the power measurement transfer function of the integration filter, can be given as

$$F(s) = \frac{1}{Ts} (1 - e^{-Ts}) \quad (21)$$

Fig. 10 shows the response of the two power measurement filters of a three-phase unbalanced system where one of the load

phases is 50% of the two other phases. Without using any kind of filtration, i.e. $F(s) = 1$, the instantaneous power has a large ripple component. When a low pass filter with a cutoff frequency of 100 rad/sec is used, the time response is fast but the power measurement suffers from a steady state ripple. When the cutoff frequency is reduced to 10 rad/sec, the ripple is attenuated but the time response is quite sluggish. The advantage of using the integration filter over the low pass filter is clear; it gives a ripple free signal with faster response. In the experimental implementation, the active and reactive power are measured using (21). However, in the linear small signal model, the time delay in (21) is approximated by a rational function using the Padé approximation. If a second order Padé approximation is used, the time delay can be expressed as

$$e^{-sT} \approx \frac{T^2/12s^2 - T/2s + 1}{T^2/12s^2 + T/2s + 1} \quad (22)$$

Substituting (22) in (21) gives

$$F(s) \approx \frac{1}{T^2/12s^2 + T/2s + 1} \quad (23)$$

It is worth noting that (23) represents a second order low pass filter with a cutoff frequency of 140 rad/sec.

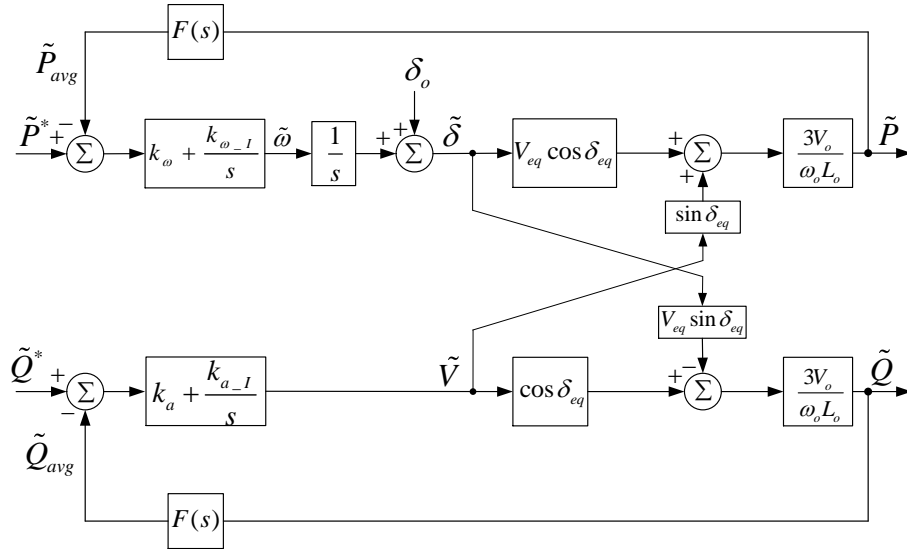


Fig. 9. Small signal model

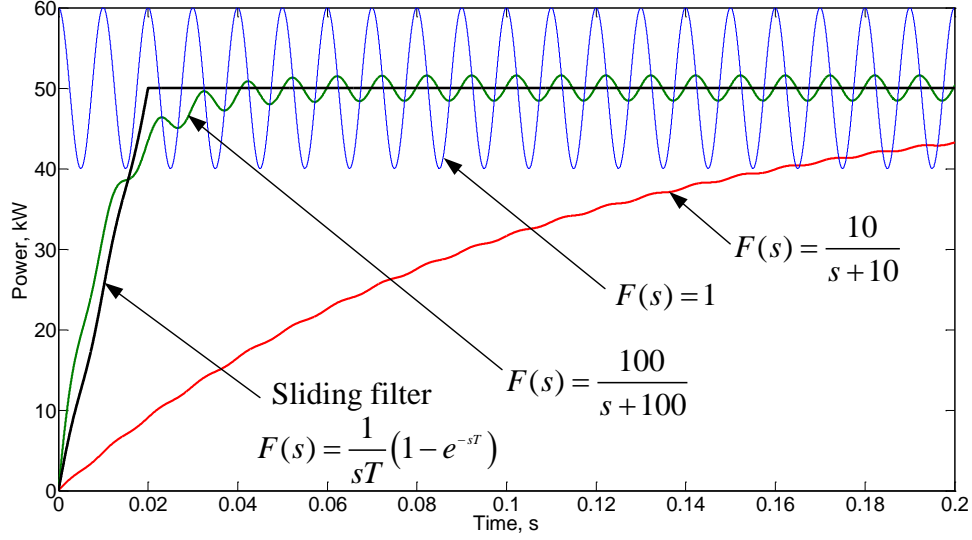


Fig. 10. Response of power calculation methods

C. Stability Analysis and Droop Coefficients Selection

The small signal model presented in Fig. 9 can be used to analyse system stability and determine the droop coefficients. During starting, which is the case that will be used to analyse stability, the angle equilibrium point is set to $\delta_{eq} = 0$, which is equivalent to starting the inverter with zero power demand $P^* = 0$. In this case, the active and reactive power controllers become fully decoupled because $\sin(\delta_{eq})$ equals zero in Fig. 9. The voltage equilibrium point is set to the nominal grid voltage $V_{eq} = V_o$. The locus of the closed loop poles of the active power small signal model when k_ω changes from 0 to 7×10^{-4} ($k_{\omega_I} = 0$) is shown in Fig. 11. The poles $\gamma_{1,2}$ are the closed loop poles when $F(s)$ is a low pass filter as given in (18) with $\omega_f = 10\text{rad/sec}$. The poles $\lambda_{1,2,3}$ are the closed loop poles when $F(s)$ is the integration filter given in (23). When the low pass filter is used to measure the power, the system is always stable. However, the root locus has a fixed distance from the imaginary axis which means that the settling time of the system is fixed and it is not affected by k_ω . On the other hand, when the integration filter is used to measure the power, the system can become unstable for large values of k_ω but there is more freedom in choosing the real value of the dominant poles to achieve the required speed of response. The locus of the closed loop poles with k_{ω_I} changes from 0 to 2×10^{-4} ($k_\omega = 1.5 \times 10^{-4}$) is also shown in Fig. 11 (enclosed by circles). The integral coefficient k_{ω_I} changes the locus of the poles very slightly and hence it has negligible effect on the dynamic response of the system.

Fig. 12 shows the root locus of the reactive power small signal model with k_a changing from 0 to 6×10^{-4} ($k_{a_I} = 0$). For both power measurement filters, the system is always stable. However, when the integration filter is used, the system step response is under-damped compared to the exponential response obtained when the low pass filter is used. In addition, the

closed loop poles are located further to the left which results in a much faster response. The locus of the poles for varying k_{a_I} (enclosed by circles) shows that it has negligible effect on the dynamic response of the system.

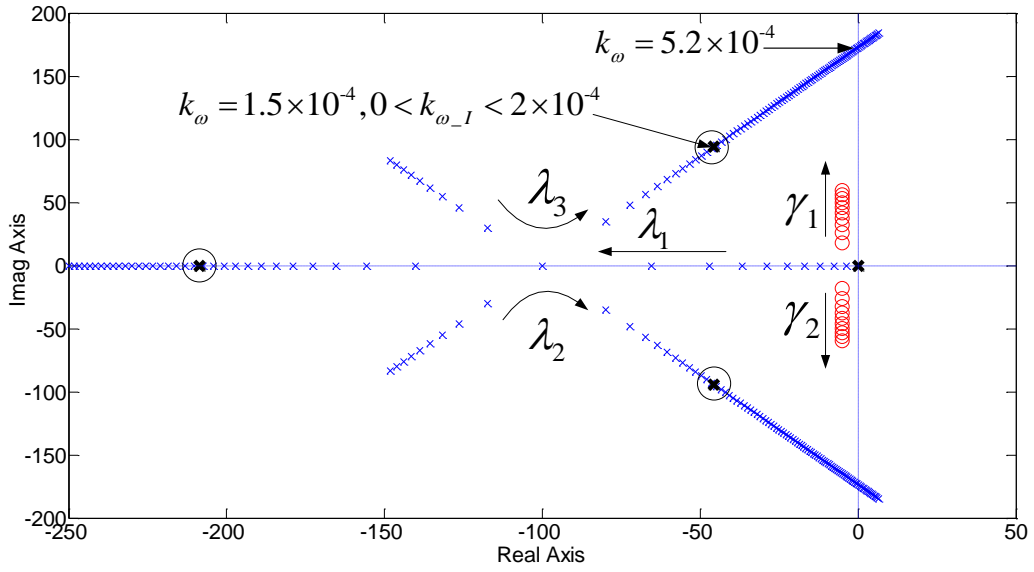


Fig. 11. Root locus diagram of the active power model, $0 < k_{\omega} < 7 \times 10^{-4}$

$k_{\omega_I} = 0$, $\gamma_{1,2}$ are the poles when LPF ($\omega_f = 10\text{rad/sec}$) is used, $\lambda_{1,2,3}$ are poles when integration filter is used. The poles enclosed by the circles represent the root locus with varying integral coefficient $0 < k_{\omega_I} < 2 \times 10^{-4}$, $k_{\omega} = 1.5 \times 10^{-4}$

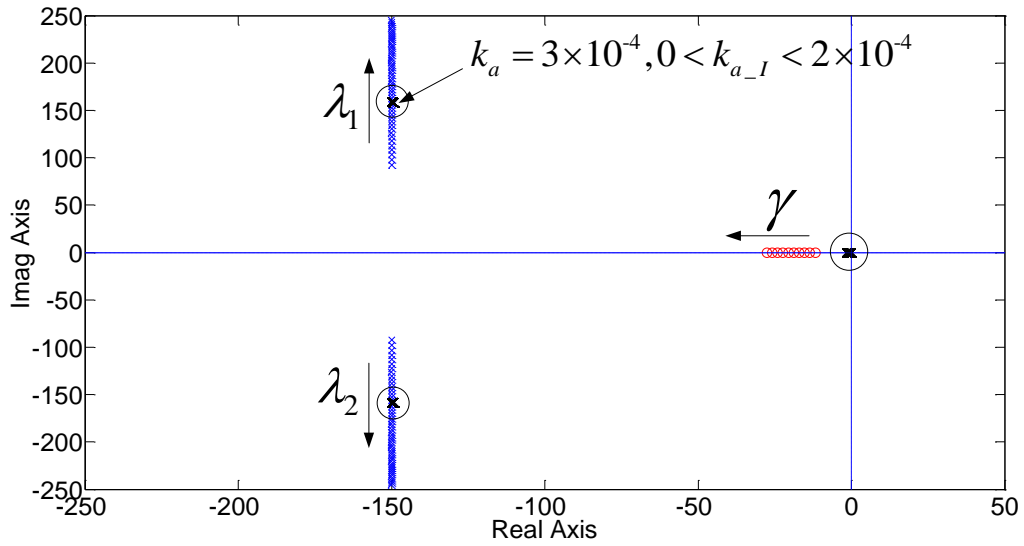


Fig. 12. Root locus diagram of the reactive power model, $0 < k_a < 6 \times 10^{-4}$, $k_{a_I} = 0$, γ is the poles when LPF ($\omega_f = 10\text{rad/sec}$) is used, $\lambda_{1,2}$ are poles when integration filter is used. The poles enclosed by the circles represent the root locus with varying integral coefficient $0 < k_{a_I} < 2 \times 10^{-4}$, $k_a = 3 \times 10^{-4}$.

The frequency drooping coefficient k_ω needs to be carefully chosen to satisfy transient requirements. The system should have a good damping ratio, ideally between 0.3 and 0.7. A number of different variables can also be examined to analyze the transient response of the controller such as circulating current as in [3]. In this design, the amount of energy that can be transferred from the grid to the inverter during a grid connection transient is examined. If the angle of the inverter output voltage lags the grid voltage by δ_o when it first connects to the grid, active power will flow from the grid to the inverter and the energy transferred will cause the DC-link voltage to rise. If the DC-link voltage is higher than the maximum limit, the protection system will trip. The trip limit V_{dc_max} is specified according to the voltage rating of the power switches of the inverter. The objective is to select the frequency droop gain k_ω so that the maximum transient energy absorbed by the inverter (caused by the presence of an initial power angle δ_o) does not cause the DC-link voltage to rise above the trip limit. If the demand power \tilde{P}^* is set to zero in Fig. 9 and by ignoring the disturbance caused by the frequency deviation and assuming $\delta_{eq} = 0$ and $V_{eq} = V_o$, the block diagram that relates the output energy (integral of power) to the disturbance δ_o is shown in Fig. 13. The proportional coefficient k_ω needs to be chosen to limit the overshoot in the output energy but without compromising relative stability. The integral coefficient k_{ω_I} does not affect the transient response as was shown earlier in the root locus diagram of Fig. 1. Table III summarizes the results of the damping ratio and the overshoot in the output energy for different values of k_ω . Increasing k_ω reduces the overshoot in the output energy but also reduces the damping ratio, which means that a compromise has to be made. The superiority of the integration filter over the low pass filter can also be seen from the results in Table III. For example, for $k_\omega = 1.5 \times 10^{-4}$, the damping ratio, when the integration filter is used, is 2.5 times more and the overshoot is 60% less than that when the low pass filter is used.

The maximum transient energy that the inverter can absorb is given by

$$E_{\max} = \frac{1}{2} C_{dc} (V_{dclink_max}^2 - V_{dclink_o}^2) \quad (24)$$

where V_{dclink_o} is the initial DC-link voltage before transient, V_{dclink_max} is the maximum allowed DC-link voltage, and C_{dc} is the DC-link capacitance. In this inverter the maximum allowed DC-link voltage, $V_{dclink_max} = 1000V$. When the inverter first connects to the AC bus, the initial DC-link voltage is $V_{dclink_o} = 750V$. According to (24), the maximum energy is therefore $E_{\max} = 438 J$. In order to prevent the DC-link voltage from rising to the maximum limit of 1000V, the overshoot transient

energy should be less than E_{\max} . The initial angle δ_o depends mainly on the closed loop phase lag that was illustrated earlier in the bode diagram in Fig. 4. Even though a phase correction can be added, due to parameter uncertainty such a phase lag may still exist which could cause transient power to be imported. During starting and before the inverter closes its output contactor (Fig. 1), the demand voltage V_c^* is synchronised with the grid voltage V_o using phase locked loop or zero crossing detection. Due to the phase lag characteristic of the closed loop system, the capacitor voltage V_c will lag the demand voltage V_c^* (and the grid voltage) by δ_o . According to Fig. 4, the phase lag at the fundamental frequency is 2.12 deg (0.037 rad). In addition, δ_o can also increase due to the measurement error in the synchronization method (phase locked loop or zero crossing detection). The drooping coefficient is set to $k_\omega = 1.5 \times 10^{-4}$. Knowing that the maximum energy that can be absorbed by the inverter is $E_{\max} = 438$ J and according to Table III, the maximum acceptable initial phase lag angle is $\delta_o = \frac{438}{8200} = 0.053$ rad. In case the synchronisation measurement causes δ_o to increase beyond this limit then a correction for the phase lag needs to be done during synchronisation.

The voltage amplitude droop coefficients k_a needs also to be chosen to satisfy transient requirements. In this design, the droop gain is set to $k_a = 3 \times 10^{-4}$ which gives a good system damping ratio of 0.6.

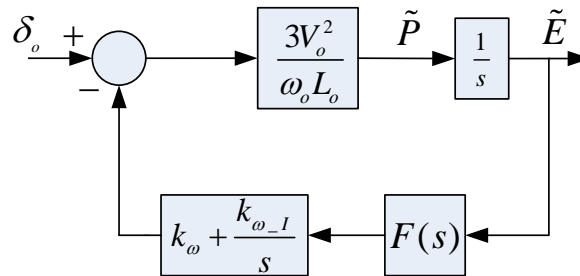


Fig. 13. Block diagram relating \dot{E} to δ_o

TABLE III
TRANSIENT RESPONSE

k_ω	Low pass filter		Integration filter	
	ζ	Energy overshoot (J)	ζ	Energy overshoot (J)
1.0×10^{-4}	0.22	$25,000 \times \delta_o$	0.64	$11,000 \times \delta_o$
1.5×10^{-4}	1.88	$20,000 \times \delta_o$	0.44	$8,200 \times \delta_o$
2.0×10^{-4}	0.16	$17,000 \times \delta_o$	0.32	$7,000 \times \delta_o$

V. SIMULATION RESULTS

A detailed model of a three-phase half-bridge PWM inverter with *LCL* filter as per Fig.1 and Table I was built in Matlab/Simulink SimPowerSystems. The controller parameters are listed in Table IV. Before the inverter connects to the grid, the inverter capacitor voltage V_c was found to lag the demand voltage V_c^* and hence the grid voltage V_o by 0.04 rad. The small signal model of Fig. 9 was also built in Simulink to compare its results with that of the detailed model. The disturbance angle δ_o is set to 0.04 rad.

Fig. 14 shows the DC-link voltage when the inverter is connecting to the grid (the integration filter is used). The imported energy caused the voltage to rise from 750 V to 950 V.

Fig. 15 shows the inverter frequency, angle and absorbed energy obtained from both the detailed model and the small signal model. It is quite clear that there is good agreement between the two models, which justifies neglecting the inverter dynamics in the small signal analysis. Fig. 15(a), (b), and (c) show the inverter frequency, angle and absorbed energy, respectively, when the power was measured using the low pass filter (LPF) method according to (18). The response is quite oscillatory and the absorbed energy is about 800 J which is much higher than the maximum allowed limit of 438J. Fig. 15(d), (e), and (f) show the inverter frequency, angle and absorbed energy, respectively, when the power was measured using the integration filter method; (equation (21) is used in the detailed model and (23) in the small signal model). The response settled in about 0.1 second. The maximum absorbed energy is 350 J. The agreement between the detailed model and the small signal model is better when using the low pass filter than when using the integration filter. This is due to the Padé approximation used to approximate the time delay in the integration filter. It is also worth noting that when a first order Padé approximation was used to model the time delay, the small signal model failed to follow the dynamics of the detailed model. This justifies using the second order Padé approximation in the small signal model. In the practical implementation of the virtual inductance, equation (21) is used.

Fig. 16 shows the maximum output current ($P=60\text{kW}$, $Q=45\text{kVAR}$) when the grid voltage includes low harmonics similar to those measured in the laboratory. The grid voltage THD was measured to be 2.0%. Fig. 16(a) shows the output current when the virtual inductance is deactivated. The current THD is 4.8%. Fig. 16(b) shows the output current when the virtual inductance is activated, the THD is dropped to 2.2%. Fig. 17 shows the grid voltage harmonics used in the simulation model and Fig. 18 shows the output current harmonics with and without the virtual inductance. The virtual inductance has significantly reduced the output current harmonics caused by the presence of grid voltage harmonics.

VI. EXPERIMENTAL RESULTS

The proposed controller was implemented experimentally for the inverter described by Fig. 1 and Table I. The inverter is supplied by a 30Ah lithium-ion battery. The controller was implemented using the Texas Instrument TMS320F2812 Fixed point Digital Signal Processor (DSP). The controller parameters of the inverter are shown in Table IV. A picture of the complete system is shown in Fig. 19.

Fig. 20 shows the DC-link voltage when the inverter is connecting to the grid. The imported energy caused the voltage to rise from 750 V to about 940 V. The response of the DC-link voltage is similar to the simulated one shown in Fig. 14.

Fig. 21 shows the grid voltage and output current. The inverter is supplying active power of 60kW and reactive power of 45kVAR. The virtual inductance is deactivated and the current THD is measured to be 6.0%. When the virtual inductance is activated, the current THD is dropped to 2.4% as shown in Fig. 22.

TABLE IV
CONTROLLER PARAMETER VALUES

Symbol	Value	Description
f_{sw}	8kHz	Inverter switching frequency
f_s	16kHz	Voltage controller sampling frequency
k_v	2.0	Capacitor voltage loop proportional gain
k_c	2.2	Capacitor current loop proportional gain
k_ω	1.5×10^{-4}	Drooping frequency coefficient
k_a	3.0×10^{-4}	Drooping voltage coefficient
$k_{\omega, I}$	5.0×10^{-5}	Integral Drooping frequency coefficient
$k_{a, I}$	1.0×10^{-4}	Integral Drooping voltage coefficient
ω_o^*	314.16 rad/sec	Nominal frequency
V_o^*	230 V (rms)	Nominal grid voltage
L_v	650 μ H	Virtual sharing inductor
ω_c	1500 rad/s	Cutoff frequency of the virtual inductance high pass filter

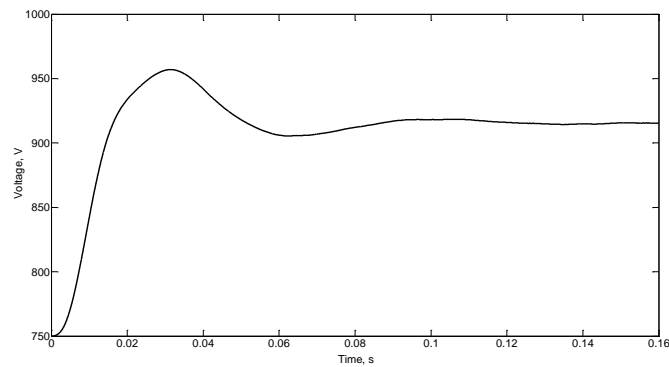


Fig. 14. Simulated Dc-link voltage when connecting to the grid

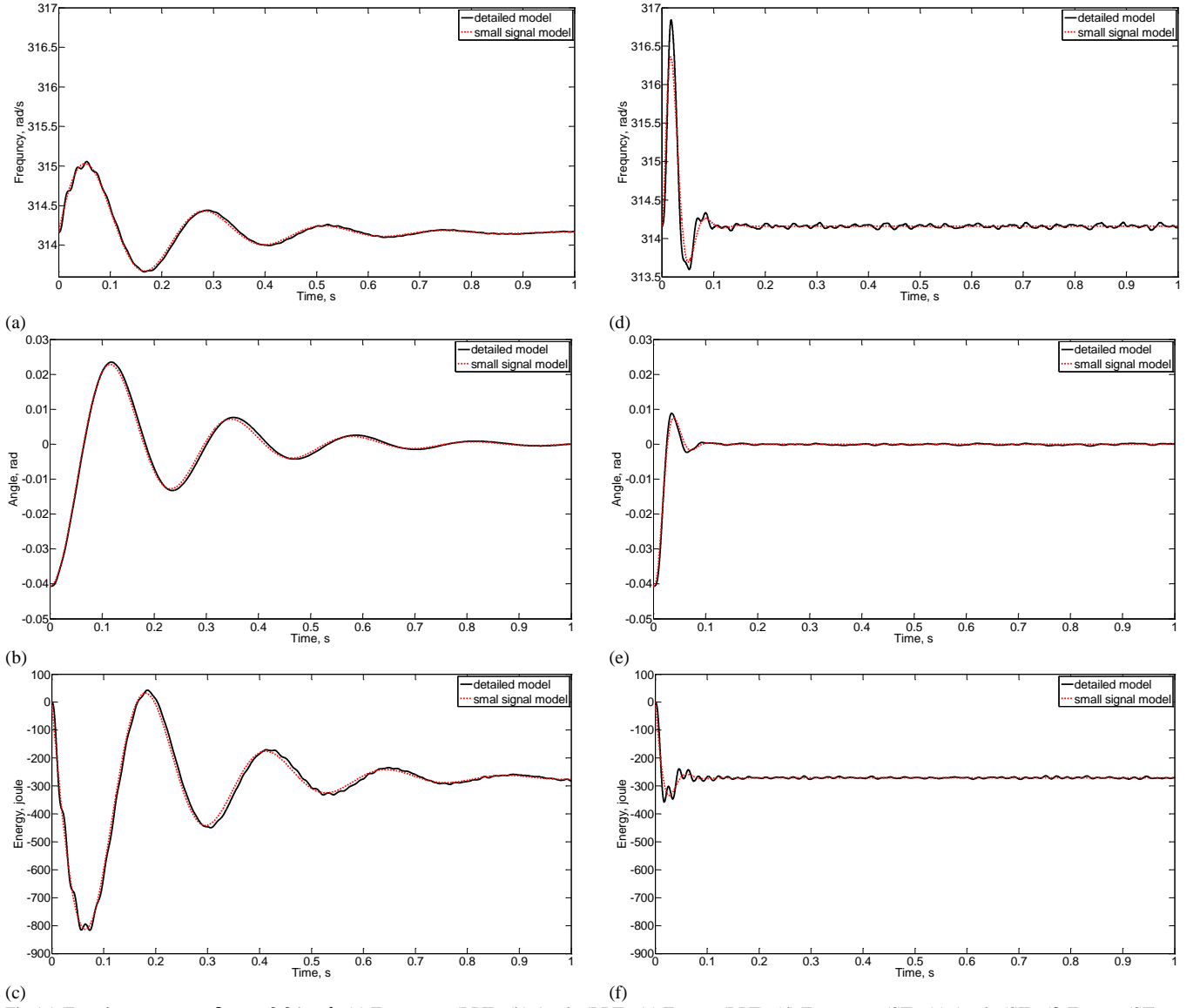


Fig.15. Transient response, $\delta_o = -0.04$ rad, (a) Frequency (LPF), (b) Angle (LPF), (c) Energy (LPF), (d) Frequency (SF), (e) Angle (SF), (f) Energy (SF),

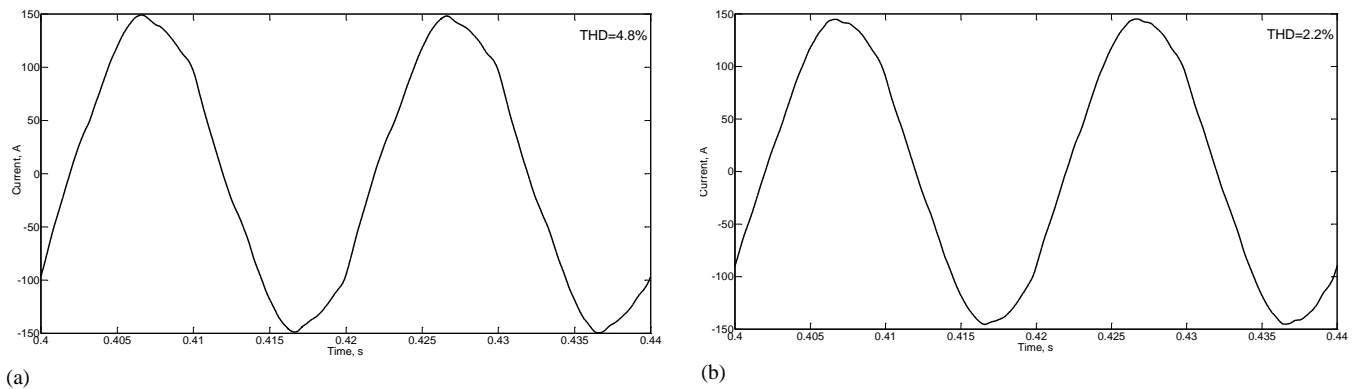


Fig. 16. Simulated output current in grid-connected mode, $P = 60$ kW, $Q = 45$ kVAR. (a) without virtual inductance (b) with virtual inductance

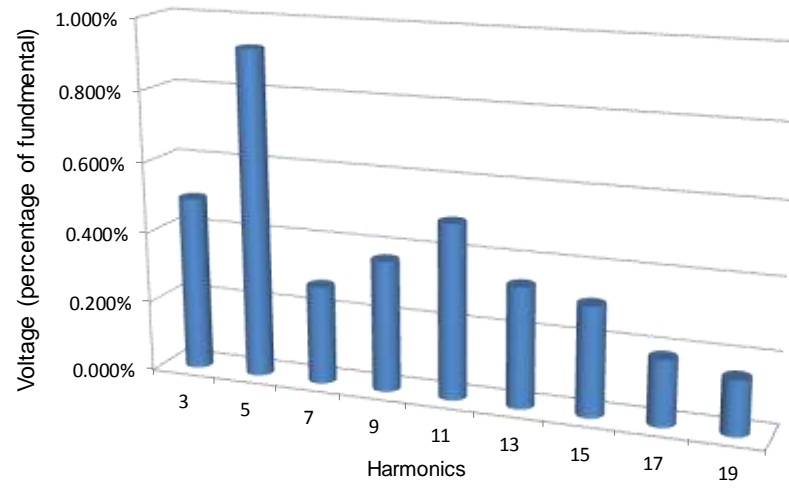


Fig. 17. Grid voltage harmonics

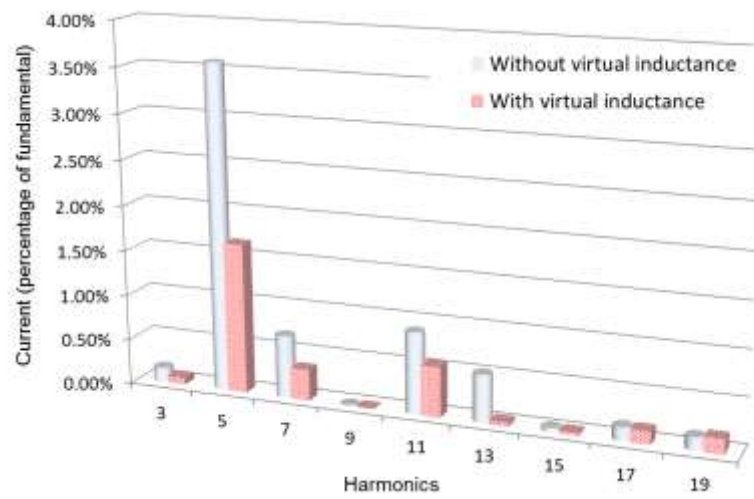


Fig. 18. Output current harmonics



Fig. 19. Experimental setup

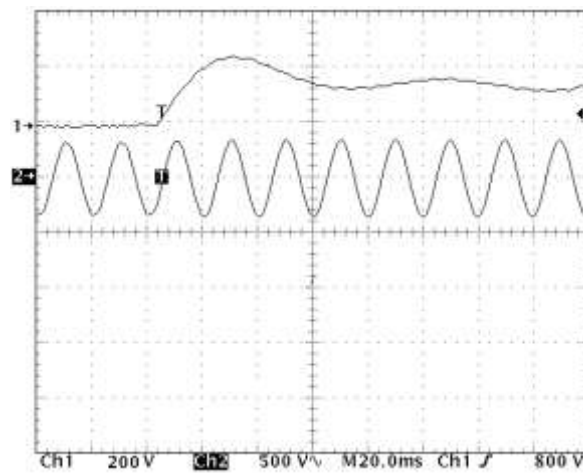


Fig. 20. Dc-link voltage (Ac coupled) and grid voltage when connecting to the grid

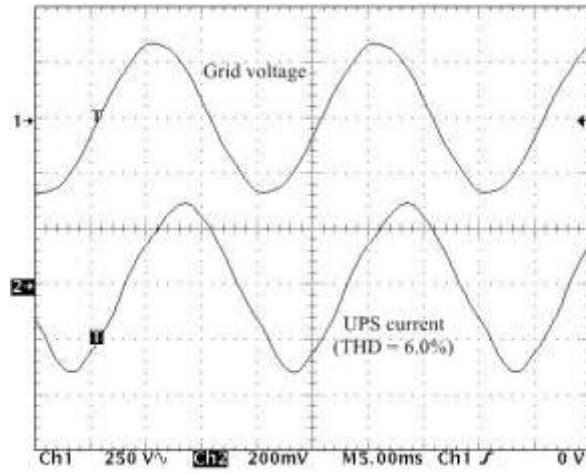


Fig. 21. Inverter output current without virtual inductance, $P = 60\text{kW}$, $Q = 45\text{kVAR}$. (current scale: 1A/2mv)

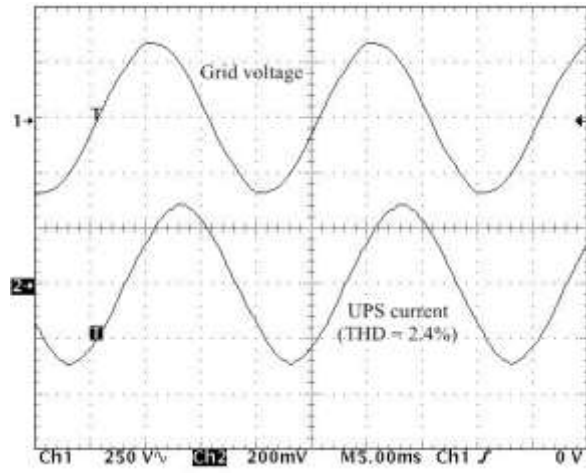


Fig. 22. Inverter output current with virtual inductance, $P = 60\text{kW}$, $Q = 45\text{kVAR}$. (current scale: 1A/2mv)

CONCLUSIONS

An improved control strategy for a droop controlled grid connected inverter has been presented. The transient response has been improved by measuring the average power using the integration method rather than using the traditional low pass filter. Virtual inductance has been found to improve the grid disturbance rejection and thus improve the output current THD. A small signal model based on transfer function approach has been developed to aid the controller design. The controller effectiveness has been validated by simulation and experiments.

REFERENCES

- [1] M. Chandorkar, D. Divan, Y. Hu, and B. Banerjee, "Novel architectures and control for distributed ups systems," in *Applied Power Electronic Conference and Exposition*, vol. 2, February 1994, pp. 683–689.
- [2] J. M. Guerrero, J. C. Vasquez, J. Matas, M. Castilla, and L.G. de Vicuna, "Control Strategy for Flexible Microgrid Based on Parallel Line-Interactive UPS Systems," *IEEE Trans. Ind. Electron.*, vol. 26, no. 3, pp. 726–736, Mar. 2009.
- [3] J. M. Guerrero, L. G. de Vicuña, J. Matas, M. Castilla, and J. Miret, "A wireless controller to enhance dynamic performance of parallel inverters in distributed generation systems," *IEEE Trans. Power Electron.*, vol. 19, no. 5, pp. 1205–1213, Sep. 2004.
- [4] M. N. Marwali, J. W. Jung, and A. Keyhani, "Control of distributed generation systems—Part II: Load sharing control," *IEEE Trans. Power Electron.*, vol. 19, no. 6, pp. 1551–1561, Nov. 2004.
- [5] J. M. Guerrero, L. G. de Vicuña, J. Matas, M. Castilla, and J. Miret, "Output Impedance Design of Parallel-Connected UPS Inverters With Wireless Load-Sharing Control," *IEEE Trans. Ind. Electron.*, vol. 52, no. 4, pp. 1126–1135, Aug. 2005.
- [6] J. M. Guerrero, J. Matas, L. G. de Vicuña, M. Castilla, and J. Miret, "Wireless-control strategy for parallel operation of distributed generation inverters," *IEEE Trans. Ind. Electron.*, vol. 53, no. 5, pp. 1461–1470, Oct. 2006.
- [7] J. M. Guerrero, J. Matas, L. G. de Vicuña, M. Castilla, and J. Miret, "Decentralized Control for Parallel Operation of Distributed Generation Inverters Using Resistive Output Impedance," *IEEE Trans. Ind. Electron.*, vol. 54, no. 2, pp. 994–1004, Apr. 2007.
- [8] Y. A. -R. I. Mohamed and E. F. El-Saadany, "Adaptive decentralized droop controller to preserve power sharing stability of paralleled inverters in distributed generation microgrids," *IEEE Trans. Power Electron.*, vol. 23, no. 6, pp. 2806–2816, Nov. 2008.
- [9] J. C. Vasquez, J. M. Guerrero, M. Liserre, and A. Mastromauro, "Voltage support provided by a droop-controlled multifunctional inverter," *IEEE Trans. Ind. Electron.*, vol. 56, no. 11, pp. 4510–4519, Nov. 2009.
- [10] J. M. Guerrero, J. C. Vasquez, J. Matas, L. G. de Vicuña, and M. Castilla "Hierarchical Control of Droop-Controlled AC and DC Microgrids—A General Approach Toward Standardization," *IEEE Trans. Ind. Electron.*, vol. 58, no. 1, pp. 158–172, Jan. 2011.
- [11] J. Kim, J. M. Guerrero, P. Rodríguez, R. Teodorescu, K. Nam, "Mode Adaptive Droop Control With Virtual Output Impedances for an Inverter-Based Flexible AC Microgrid," *IEEE Trans. Ind. Electron.*, vol. 26, no. 3, pp. 689–701, Mar. 2011.
- [12] E. A. Coelho, P. C. Cortizo, and P. F. Garcia, "Small signal stability for single phase inverter connected to stiff AC system," in *Conf. Rec. 34th IEEE IAS Annu. Meeting*, 1999, vol. 4, pp. 2180–2187.
- [13] J. C. Vasquez, J. M. Guerrero, A. Luna, P. Rodríguez, and R. Teodorescu, "Adaptive Droop Control Applied to Voltage-Source Inverters Operating in Grid-Connected and Islanded Modes," *IEEE Trans. Ind. Electron.*, vol. 56, no. 10, pp. 4088–4096, Oct. 2009.
- [14] T. L. Vandoorn, J. D. M. De Kooning, B. Meersman, J. M. Guerrero and L. Vandevelde, "Voltage-Based Control of a Smart Transformer in a Microgrid," *IEEE Trans. Ind. Electron.*, 2011.
- [15] M. Savaghebi, A. Jalilian, J. C. Vasquez, and J. M. Guerrero, "Autonomous Voltage Unbalance Compensation in an Islanded Droop-Controlled Microgrid," *IEEE Trans. Ind. Electron.*, 2012.
- [16] J. He, Y. W. Li, Member, and M. S. Munir, "A Flexible Harmonic Control Approach Through Voltage-Controlled DG–Grid Interfacing Converters," *IEEE Trans. Ind. Electron.*, vol. 59, no. 1, pp. 444–455, Jan. 2012.
- [17] S. M. Sharkh and M. Abu-Sara, "Digital current control of utility connected two-level and three-level PWM voltage source inverters," *European Power Electronic Journal*, vol. 14 No. 4, 2004, pp. 13–18.

- [18] M. A. Abusara and S.M. Sharkh, "Digital control of a three-phase grid connected inverter," *Int. J Power Electronics*, vol. 3 No. 3, 2011, pp. 299-319.
- [19] M. A. Abusara and S. M. Sharkh, "Design and Control of a Three-Phase Grid Connected Interleaved Inverter," *IEEE Trans. Power Electron.*, vol. 28, no. 2, pp. 748–764, Feb. 2013.
- [20] M. Liserre, R. Theodorescu, and F. Blaabjerg, "Stability of photovoltaic and wind turbine grid-connected inverters for a large set of grid impedance values," *IEEE Trans. Power Electron.*, vol. 21, no. 1, pp. 263–272, Jan. 2006.
- [21] S. Cobrecas, E. Bueno, F. J. Rodriguez, F. Huerta, and P. Rodriguez, "Influence analysis of the effects of an inductive-resistive weak grid over L and LCL filter current hysteresis controllers," in *Proc. 2007 Eur. Conf. Power Electron. Appl.*, pp. 1–10
- [22] H. Avelar, W. Parreira, J. Vieira, L. de Freitas, and E. Coelho, "A state equation model of a single-phase grid-connected inverter using a droop control scheme with extra phase shift control action," *IEEE Trans. Ind. Electron.*, vol. 59, no. 3, pp. 1527-1537, Mar. 2012.
- [23] E. P. de Paiva, J. B. Vieira, Jr., L. C. de Freitas, V. J. Farias, and E. A. A. Coelho, "Small signal analysis applied to a single phase inverter connected to stiff AC system using a novel improved power controller," in *Proc. 20th Annu. IEEE APEC*, Jun. 2005, vol. 2, pp. 1099–1104.
- [24] E. P. de Paiva, J. B. Vieira, Jr., L. C. de Freitas, V. J. Farias, and E. A. A. Coelho, "An improved power controller for a single phase grid connected inverter with root locus analysis," *SOBRAEP*, vol. 14, pp. 17–23, Feb. 2009.
- [25] M. A. Abusara, and S. M. Sharkh, "Control of line interactive UPS systems in a Microgrid," in *Proc. IEEE ISIE*, 2011, pp. 1433–1440.
- [26] M. A. Abusara, J. M. Guerrero, and S. M. Sharkh, "Line Interactive UPS for Microgrids," *IEEE Trans. Ind. Electron.*, vol. 61, no. 3, pp. 1292-1300, Mar. 2014.
- [27] Trujillo Rodriguez, C.; Velasco de la Fuente, D.; Garcera, G.; Figueres, E.; Guacaneme Moreno, J.A., "Reconfigurable Control Scheme for a PV Microinverter Working in Both Grid-Connected and Island Modes," " *IEEE Trans. Ind. Electron*, vol.60, no.4, pp.1582,1595, April 2013
- [28] Velasco de la Fuente, D.; Rodríguez, C.L.T.; Garcera, G.; Figueres, E.; Gonzalez, R.O., "Photovoltaic Power System With Battery Backup With Grid-Connection and Islanded Operation Capabilities," " *IEEE Trans. Ind. Electron* , vol.60, no.4, pp.1571,1581, April 2013
- [29] Avelar, H.J.; Parreira, W.A.; Vieira, J.B.; de Freitas, L.C.G.; Alves Coelho, E.A., "A State Equation Model of a Single-Phase Grid-Connected Inverter Using a Droop Control Scheme With Extra Phase Shift Control Action," " *IEEE Trans. Ind. Electron*, vol.59, no.3, pp.1527,1537, March 2012.
- [30] Jinwei He; Yun Wei Li, "Hybrid Voltage and Current Control Approach for DG-Grid Interfacing Converters With LCL filters," " *IEEE Trans. Ind. Electron*, vol.60, no.5, pp.1797,1809, May 2013.
- [31] C. Zou, B. Liu, S. Duan, and R. Li, "Stationary Frame Equivalent Model of Proportional-Integral Controller in dq Synchronous Frame," *IEEE Trans. Power Electron.*, vol. 29, no. 9, pp. 4461–4465, Jan. 2014.